Pré-Publicações do Departamento de Matemática
Universidade de Coimbra
Preprint Number 10–30

A SEGMENTATION MODEL USING IMAGE GRADIENT INFORMATION AND APPLICATIONS TO ENDOSCOPIC IMAGES

ISABEL N. FIGUEIREDO, JUAN MORENO, SURYA PRASATH AND PEDRO FIGUEIREDO

Abstract: In this paper a variational segmentation model is proposed. It is a generalization of the Chan and Vese model, for the scalar and vector-valued cases. It incorporates extra terms, depending on the image gradient, and aims at approximating the smoothed image gradient norm, inside and outside the segmentation curve, by mean constant values. As a result, a flexible model is obtained. It segments, more accurately, any object displaying many oscillations in its interior. In effect, an external contour of the object, as a whole, is achieved, together with internal contours, inside the object. The existence of solution to this model is addressed and proved. For determining the approximate solution a Levenberg-Marquardt Newton-type optimization method is applied to the finite element discretization of the model. Experiments on synthetic images and *in vivo* medical endoscopic images (displaying aberrant colonic crypt foci) illustrate the efficacy of this model. Moreover, comparisons with the Chan and Vese segmentations show the advantage of the proposed model in terms of accuracy.

Keywords: segmentation, variational methods.
AMS Subject Classification (2010): 65K10, 49J27, 49M15.

1. Introduction and motivation

Image segmentation is a principal issue in image processing. It aims at partitioning an image into a finite number of disjoint objects, and at identifying the boundaries separating them. It is a subject of extreme importance in computer vision. Recently, there has been a growing interest on automatic segmentation of medical images.

There are many types of segmentation methods, and some of the most effective are variational or PDE (partial differential equation) based methods (see for instance [3, 8, 18]). Among these we refer in particular the active contour/snake model (see [14]) and the geodesic/geometric active contour models (see [5, 15, 17]), which are enhancements of the previous model. These are all based on techniques of curve evolution and use an edge-detector function,

Received September 09, 2010.
This work was partially supported by the research project UTAustin/MAT/0009/2008 of the UT Austin | Portugal Program (http://www.utaustinportugal.org/).

depending on the gradient of the given image, to stop the evolving curve on the boundary of the object to be segmented. Another fundamental approach is the variational model defined by the Mumford-Shah's functional [19]. In particular, the Chan and Vese model (for the scalar or vector-valued cases [9, 7]) is a simplified version of this Mumford-Shah's functional, that is formulated in a level set framework [20, 21]. This model is also included in the so-called class of active contours without edges model, in contrast with the above mentioned snake or geodesic/geometric active contours, because it does not contain any edge detector and neither is the gradient of the image incorporated in the model. For the case of a scalar image, the Chan and Vese model (see [9]) seeks to approximate an image by a function taking only two values, representing the mean intensity inside and outside the segmented region (for a vector-valued image it approximates each component of the image in a similar way, see [7]). Like this, a binary segmentation is achieved: the image is partitioned into two regions (the detected objects and the background) and the segmentation curve is the boundary between these two regions.

In [4] a modified version of the Chan and Vese model [9] is introduced. Based on a redefinition of [9], as a global convex minimization problem (see [6]), in [4] this redefinition is modified (with the motivation of a fast computation of a global minimum) to incorporate information from an edge detector. More precisely, this modification includes a weighted total variation term, whose weight function can be chosen to be an edge detector, depending on the image gradient. In this way, as mentioned in [13], "... the model is more likely to favor segmentation along curves where the edge detector function is minimal".

In this paper we propose a generalization of the Chan and Vese model (for the scalar and vector-valued cases [9, 7]), by adding to the minimization functional extra terms, that depend on the image gradient (see (1), (2) and (5), in section 2). By doing this we incorporate more information about the input image in the segmentation model, and consequently we expect an enhancement of the model. Unlike the above mentioned paper [4], the new extra terms are not edge-detectors, but rather fitting terms that intend to approximate the smoothed image gradient norm, inside and outside the segmentation curve, by mean constant values. The goal is to create a model able to segment, more accurately, any object displaying many oscillations in its interior. In effect in our experiments, either synthetic or endoscopic

images (see section 5), an external contour of this type object, as a whole, is achieved, together with internal contours, inside the object.

It is worth mentioning, that for the particular medical endoscopic images presented in this paper, containing *in vivo* colonic aberrant crypt foci, the physician requirements were also the main inducement for defining this segmentation model. In effect, from the medical point of view the main goal is to achieve a segmentation able to detect the macro (external) contour of each aberrant focus (each focus is a set of several crypts, which are more darkly stained than normal crypts, see [22]), as well as, if possible, the micro (internal) contours inside the focus. These interior contours should segment the crypt's orifices, whose shapes are important to recover, for medical research and possible diagnostic assessments (according to endoscopic criteria, see for instance [1, 22, 23], the shapes of the crypt's openings are classified in three main types: type I for round, oval or semi-circular lumens, type II for asteroidal or slit-like lumens, and type III for compressed and ill-defined lumens).

In the literature we found out a related paper, [25], where the square of the gradient norm of a smoother version of an image is considered as the input datum for the Chan and Vese model [9]. In addition, applications to some bone computed tomography (CT) images are described. We remark however that for the endoscopic medical images presented in our paper, using only the gradient norm channels as input data, did not produce good segmentation results (see Figures 4 (e) and 5 (e)).

This paper is organized as follows. After this introduction, the following section 2 details the proposed model and its generalization to vector-valued images. Then, in section 3 we prove the existence of minimizers, by reformulating the model and using properties of bounded variation spaces. A global minimization result is also stated (it results directly from an analogous global minimizer result for the Chan and Vese model, demonstrated in [6]). Section 4 briefly describes the numerical approximation employed (a Levenberg-Marquardt Newton-type optimization method applied to the model finite element discretization, as in [11]). Section 5 reports the results of the experiments conducted on synthetic images and medical endoscopic images. Comparisons with the Chan and Vese segmentations highlight the better performance of the new proposed model. Finally some conclusions and future work.

2. Description of the model

Let Ω be a bounded open set of $\mathbb{R}^2$, $I : \overline{\Omega} \longrightarrow \mathbb{R}$ a scalar function representing a given image, $|\nabla I|^s$ a smoothed version of its gradient norm, and C a curve in Ω, symbolizing the segmentation curve of the region in Ω to segment.

We define the variational segmentation functional

$$\begin{aligned} &F(c,d,C) := \mu\,\text{Length}\,(C) + \eta\,\text{Area}\,(\text{inside}\,C) + \\ &\lambda_{in}\int_{\text{inside}\,(C)} |I-c_{in}|^2\,dx + \lambda_{out}\int_{\text{outside}\,(C)} |I-c_{out}|^2\,dx + \\ &\overline{\lambda}_{in}\int_{\text{inside}\,(C)} \left||\nabla I|^s - d_{in}\right|^2 dx + \overline{\lambda}_{out}\int_{\text{outside}\,(C)} \left||\nabla I|^s - d_{out}\right|^2 dx. \end{aligned} \tag{1}$$

Here $c := (c_{in}, c_{out})$ and $d := (d_{in}, d_{out})$ are the unknown averages of I and $|\nabla I|^s$, respectively, inside (for the subscript in) and outside (for the subscript out) the unknown segmentation curve C; μ and η are two nonnegative fixed regularizing parameters (μ and η penalize the length of the boundaries of C and the area inside C, respectively) ; λ_{in}, λ_{out}, $\overline{\lambda}_{in}$, $\overline{\lambda}_{out}$ are nonnegative fixed parameters weighting the fitting terms (they are scale parameters, in the sense the bigger they are the more details will be captured). In the sequel we also denote $\lambda := (\lambda_{in}, \lambda_{out})$ and $\overline{\lambda} := (\overline{\lambda}_{in}, \overline{\lambda}_{out})$.

Let now the curve $C \subset \Omega$ be represented by the 0-level set of a Lipschitz function $\phi : \Omega \to \mathbb{R}$, which means

$$\begin{aligned} C &:= \{x \in \Omega :\ \phi(x) = 0\} \\ \text{inside}\,(C) &:= \{x \in \Omega :\ \phi(x) > 0\} \\ \text{outside}\,(C) &:= \{x \in \Omega :\ \phi(x) < 0\}. \end{aligned}$$

Then the level set formulation of (1) is

$$\begin{aligned} F(c,d,\phi) \;:=\; &\mu\int_\Omega \delta(\phi)|\nabla\phi|\,dx + \eta\int_\Omega H(\phi)\,dx + \\ &\lambda_{in}\int_\Omega |I-c_{in}|^2\,H(\phi)\,dx + \lambda_{out}\int_\Omega |I-c_{out}|^2\,\big(1-H(\phi)\big)\,dx + \\ &\overline{\lambda}_{in}\int_\Omega \left||\nabla I|^s - d_{in}\right|^2 H(\phi)\,dx + \overline{\lambda}_{out}\int_\Omega \left||\nabla I|^s - d_{out}\right|^2 \big(1-H(\phi)\big)\,dx, \end{aligned} \tag{2}$$

where H is the Heaviside function ($H(z) := 1$ if $z \geq 0$, $H(z) := 0$ if $z < 0$), and $\delta(z) := \frac{d}{dz}H(z)$ is the Dirac delta function in the sense of distributions.

We address the problem

$$\min_{(c,d,\phi)} F(c,d,\phi). \tag{3}$$

We remark that when $\overline{\lambda}_{in} = 0 = \overline{\lambda}_{out}$, then (3) coincides with the Chan and Vese model [9].

By fixing ϕ and minimizing with respect to the unknown averages c_{in}, c_{out}, d_{in}, d_{out}, separately, it is found that these are functions of ϕ and verify

$$\begin{aligned} c_{in}(\phi) &= \tfrac{\int_\Omega I\, H(\phi)\, dx}{\int_\Omega H(\phi)\, dx}, \qquad & c_{out}(\phi) &= \tfrac{\int_\Omega I\, \left(1-H(\phi)\right) dx}{\int_\Omega \left(1-H(\phi)\right) dx} \\ d_{in}(\phi) &= \tfrac{\int_\Omega |\nabla I|^s\, H(\phi)\, dx}{\int_\Omega H(\phi)\, dx}, \qquad & d_{out}(\phi) &= \tfrac{\int_\Omega |\nabla I|^s\, \left(1-H(\phi)\right) dx}{\int_\Omega \left(1-H(\phi)\right) dx}. \end{aligned} \tag{4}$$

A straightforward generalization of the functional (2) to vector-valued images with n components, *i.e.* $I = (I_1, \ldots, I_n) : \overline{\Omega} \longrightarrow \mathbb{R}^n$, is (compare with the model defined in [7])

$$\begin{aligned} F(c,d,\phi) \;:=\; & \mu \int_\Omega \delta(\phi)|\nabla\phi|\, dx + \eta \int_\Omega H(\phi)\, dx + \\ & \tfrac{1}{n}\textstyle\sum_{i=1}^n \Big(\int_\Omega \lambda^i_{in}|I_i - c^i_{in}|^2\, H(\phi)\, dx + \int_\Omega \lambda^i_{out}|I_i - c^i_{out}|^2 \left(1 - H(\phi)\right) dx \Big) + \\ & \tfrac{1}{n}\textstyle\sum_{i=1}^n \Big(\int_\Omega \overline{\lambda}^i_{in}\big||\nabla I_i|^s - d^i_{in}\big|^2\, H(\phi)\, dx + \int_\Omega \overline{\lambda}^i_{out}\big||\nabla I_i|^s - d^i_{out}\big|^2 \left(1 - H(\phi)\right) dx \Big), \end{aligned} \tag{5}$$

where $c := (c_{in}, c_{out})$ and $d := (d_{in}, d_{out})$ are now defined by $c_{in} := (c^i_{in})_{i=1}^n$, $d_{in} := (d^i_{in})_{i=1}^n$, $c_{out} := (c^i_{out})_{i=1}^n$, $d_{out} := (d^i_{out})_{i=1}^n$, and λ^i_{in}, λ^i_{out} $\overline{\lambda}^i_{in}$, $\overline{\lambda}^i_{out}$ are again nonnegative fixed fitting term parameters, for $i = 1, \ldots, n$. We also denote $\lambda := (\lambda^i)_{i=1}^n$ with $\lambda^i := (\lambda^i_{in}, \lambda^i_{out})$, and $\overline{\lambda} := (\overline{\lambda}^i)_{i=1}^n$ with $\overline{\lambda}^i := (\overline{\lambda}^i_{in}, \overline{\lambda}^i_{out})$.

In the sequel we consider as well the following modified objective functional, either for (2) or (5), with two extra regularizing terms (see [11], where the same regularization is proposed)

$$F_{\alpha\beta}(c,d,\phi) := F(c,d,\phi) + \frac{\beta}{4}\int_\Omega \left(|\nabla\phi|^2 - 1\right)^2 dx + \frac{\alpha}{2}\int_\Omega |\nabla\phi|^2\, dx, \tag{6}$$

where $\beta \geq 0$ and $\alpha \geq 0$ are two small positive fixed parameters. The term $\frac{\beta}{4}\int_\Omega \left(|\nabla\phi|^2 - 1\right)^2 dx$ simply penalizes the deviation of the slope of the level set function from unity, which gives a well-defined level-set function (similarly to a signed distance function, which also attempts to maintain a slope of 1). The term $\frac{\alpha}{2}\int_\Omega |\nabla\phi|^2 dx$ is a Tikhonov like regularization.

3. Existence of solution

In this section we first prove there exists a solution to the minimization problem (3), when the objective functional is defined by (2) for the scalar case, by (5) for the vector-valued case or by (6) for the regularized case (either scalar or vector-valued). We remark, however, that this proof also applies directly to the Chan and Vese model (as suggested, but not demonstrated,

in [9], p.269), since (2), (5) or (6) reduce to the Chan and Vese functional, by choosing the $\overline{\lambda}$ parameters in the gradient norm terms, and the regularizing parameters, α and β, equal to zero. Secondly, we show that, when the objective functional is defined either by (2) or (5), the segmentation problem can be reformulated as a similar problem which has a global minimizer (the proof relies on analogous arguments to those employed in [6], for the Chan and Vese model).

For the first claim we need to recall a definition and some properties of functions with bounded variation (see below definition 3.1 and theorems 3.1, 3.2, 3.3: cf. [2, 12], for example, for a detailed explanation of these concepts).

Definition 3.1. *Let $\Omega \subset \mathbb{R}^n$ be an open set and $f \in L^1(\Omega)$ (in this paper $n = 2$). Define*

$$\int_\Omega |Df| := \sup_{\phi \in \Phi} \left\{ \int_\Omega f \, div\phi \, dx \right\}$$

where $\Phi = \left\{ \phi \in C_0^1(\Omega, \mathbb{R}^2) : |\phi(x)| \leq 1 \text{ in } \Omega \right\}$. A function $f \in L^1(\Omega)$ is said to have bounded variation in Ω, if $\int\limits_\Omega |Df| < +\infty$. In particular, if $f \in W^{1,1}(\Omega)$, then $\int\limits_\Omega |Df| = \int\limits_\Omega |\nabla f(x)| dx$, where ∇f is the gradient of f in the sense of distributions. $BV(\Omega)$ is the space of all functions in $L^1(\Omega)$ with bounded variation. Under the norm $\|f\|_{BV(\Omega)} = \|f\|_{L^1(\Omega)} + \int_\Omega |Df|$, $BV(\Omega)$ is a Banach space.

Theorem 3.1. *([2], p.402) If $f \in BV(\Omega)$, then for a.e. $t \in \mathbb{R}$, the level set $E_t := \{x \in \Omega : \ f(x) > t\}$ has finite perimeter, i.e., its characteristic function $\chi_{E_t} \in BV(\Omega)$ (Note: by definition a Borel subset E of $\mathbb{R}^n$ is called a set of finite perimeter, when its characteristic function $\chi_E \in BV(\Omega)$).*

Theorem 3.2. *([2], p.378) Let Ω be a 1-regular open bounded subset of $\mathbb{R}^n$. Then for all p, $1 \leq p < \frac{n}{n-1}$, the embedding $BV(\Omega) \subset L^p(\Omega)$ is compact.*

Theorem 3.3. *([2], p.372) Let $(f_k)_{k \in \mathbb{N}}$ be a sequence in $BV(\Omega)$ strongly converging to some $f \in L^1(\Omega)$ and satisfying $\sup_{k \in \mathbb{N}} \int_\Omega |Df_k| < +\infty$. Then, $f \in BV(\Omega)$, $\int_\Omega |Df| \leq \liminf_{k \to +\infty} \int_\Omega |Df_k|$, and f_k weakly converges to f in $BV(\Omega)$.*

We now make use of the above properties to reformulate problem (3). Let ω denote the set corresponding to the region inside (C), which means $\omega := \{x \in \Omega : \ \phi(x) > 0\}$. Then using χ_ω, the characteristic function of ω

($\chi_\omega(x) = 1$, if $x \in \omega$, and $\chi_\omega(x) = 0$, if $x \notin \omega$), and due to definition 3.1 and theorem 3.1 we reformulate the functional (2) as

$$\begin{aligned} F(\chi_\omega) \;:=\; & \mu \int_\Omega |\nabla \chi_\omega|\, dx + \eta \int_\Omega \chi_\omega\, dx + \\ & \lambda_{in} \int_\Omega |I - c_{in}(\chi_\omega)|^2\, \chi_\omega\, dx + \lambda_{out} \int_\Omega |I - c_{out}(\chi_\omega)|^2 \left(1 - \chi_\omega\right) dx + \\ & \overline{\lambda}_{in} \int_\Omega \left||\nabla I|^s - d_{in}(\chi_\omega)\right|^2 \chi_\omega\, dx + \overline{\lambda}_{out} \int_\Omega \left||\nabla I|^s - d_{out}(\chi_\omega)\right|^2 \left(1 - \chi_\omega\right) dx, \end{aligned} \tag{7}$$

with (compare to (4))

$$\begin{aligned} c_{in}(\chi_\omega) &= \tfrac{\int_\Omega I\, \chi_\omega\, dx}{\int_\Omega \chi_\omega\, dx}, & c_{out}(\chi_\omega) &= \tfrac{\int_\Omega I \left(1-\chi_\omega\right) dx}{\int_\Omega \left(1-\chi_\omega\right) dx} \\ d_{in}(\chi_\omega) &= \tfrac{\int_\Omega |\nabla I|^s\, \chi_\omega\, dx}{\int_\Omega \chi_\omega\, dx}, & d_{out}(\chi_\omega) &= \tfrac{\int_\Omega |\nabla I|^s \left(1-\chi_\omega\right) dx}{\int_\Omega \left(1-\chi_\omega\right) dx}. \end{aligned} \tag{8}$$

In addition, the minimization problem (3) is redefined as

$$\min_{\chi_\omega \in BV(\Omega)} F(\chi_\omega). \tag{9}$$

We remark that a similar reformulation to (7) holds true for the functionals (5) and (6).

Proposition 3.1. *There exists a solution to the minimization problem* (9)*, where the objective functional is a redefinition of* (2) *(or of* (5) *or* (6)*), by means of characteristic functions.*

Proof: The proof is presented only for the objective functional (2) (the generalization to the functionals (5) and (6) is straightforward, so it is omitted).

Set $m := \inf_{\chi_\omega \in BV(\Omega)} F(\chi_\omega)$. If $m = +\infty$, there is nothing to prove. So, let's suppose that $m < +\infty$. Let $\{\chi_{\omega_k}\}_{k=1}^{\infty}$ be a minimizing sequence for F, *i.e.*

$$F(\chi_{\omega_k}) \xrightarrow{k\to\infty} m.$$

Then, from (7)

$$F(\chi_{\omega_k}) \geq\; \mu \int\limits_\Omega |\nabla \chi_{\omega_k}| dx,$$

and consequently

$$\sup_{k\in\mathbb{N}} \int\limits_\Omega |\nabla \chi_{\omega_k}| dx < +\infty. \tag{10}$$

But, because $\chi_{\omega_k} \in W_0^{1,1}(\Omega)$ and Ω is bounded we can apply Poincaré inequality to obtain

$$\|\chi_{\omega_k}\|_{L^1(\Omega)} \leq C \|\nabla \chi_{\omega_k}\|_{L^1(\Omega)} = C \int\limits_\Omega |D\chi_{\omega_k}| \leq \widetilde{C} \tag{11}$$

where C and $\widetilde{C}$ are constants independent of ω_k. Thus, from (10) and (11) we conclude that

$$\sup_{k\in\mathbb{N}} \|\chi_{\omega_k}\|_{BV(\Omega)} < +\infty.$$

Then $\{\chi_{\omega_k}\}_{k=1}^{\infty}$ is bounded in $BV(\Omega)$ and due to theorem 3.2, there is a subsequence of $\{\chi_{\omega_k}\}_{k=1}^{\infty}$, that we also denote by $\{\chi_{\omega_k}\}_{k=1}^{\infty}$, strongly convergent to an element $f \in L^1(\Omega)$. Since χ_{ω_k} is either 1 or 0, f is either 1 or 0 *a.e.* in Ω. Therefore we may view f as the characteristic function, χ_E, of a set E. But then, by theorem 3.3, $f \in BV(\Omega)$ and $\int_\Omega |Df| \leq \liminf_{k\to+\infty} \int_\Omega |Df_k|$. This latter inequality leads to

$$F(\chi_E) \leq \liminf_{k\to\infty} F(\chi_{\omega_k}) = m. \tag{12}$$

In effect, we have that

$$\lim_{k\to\infty} \overline{F}(\chi_{\omega_k}) = \overline{F}(\chi_E), \quad \text{with} \quad \overline{F}(\chi_{\omega_k}) := F(\chi_{\omega_k}) - \mu \int_\Omega |\nabla \chi_{\omega_k}|\, dx.$$

because $\{\chi_{\omega_k}\}_{k=1}^{\infty}$ strongly converges to χ_E in $L^1(\Omega)$. Since $\chi_E \in BV(\Omega)$, we conclude, from (12), $F(\chi_E) = m$ and this ends the proof. ∎

Proposition 3.2. *For any fixed $c = (c_{in}, c_{out})$, $d = (d_{in}, d_{out})$, the problem $\min_\phi F(c, d, \phi)$ with F defined by (2) or (5) (which is a nonconvex minimization problem), can be reformulated as the following convex constrained problem*

$$\min_{0\leq\phi\leq 1} G(c, d, \phi), \tag{13}$$

where the objective functional G is

$$\begin{aligned} G(c,d,\phi) \;:=\; & \mu \textstyle\int_\Omega |\nabla\phi|\, dx + \eta \int_\Omega \phi\, dx + \\ & \lambda_{in} \textstyle\int_\Omega |I - c_{in}|^2 \phi\, dx - \lambda_{out} \int_\Omega |I - c_{out}|^2 \phi\, dx + \\ & \overline{\lambda}_{in} \textstyle\int_\Omega \left||\nabla I|^s - d_{in}\right|^2 \phi\, dx - \overline{\lambda}_{out} \int_\Omega \left||\nabla I|^s - d_{out}\right|^2 \phi\, dx, \end{aligned} \tag{14}$$

for (2), and for (5)

$$\begin{aligned} G(c,d,\phi) \;:=\; & \mu \textstyle\int_\Omega |\nabla\phi|\, dx + \eta \int_\Omega \phi\, dx + \\ & \tfrac{1}{n} \textstyle\sum_{i=1}^n \left(\lambda^i_{in} \int_\Omega |I_i - c^i_{in}|^2 \phi\, dx - \lambda_{out} \int_\Omega |I_i - c^i_{out}|^2 \phi\, dx\right) + \\ & \tfrac{1}{n} \textstyle\sum_{i=1}^n \left(\overline{\lambda}^i_{in} \int_\Omega \left||\nabla I_i|^s - d^i_{in}\right|^2 \phi\, dx - \overline{\lambda}^i_{out} \int_\Omega \left||\nabla I_i|^s - d^i_{out}\right|^2 \phi\, dx\right) \end{aligned} \tag{15}$$

for (5). Then, the segmented region to be recovered is defined by the set $\{x \in \Omega :\ \phi(x) \geq s\}$ for a.e. $s \in [0, 1]$.

In addition, problem (13) has the same set of minimizers as the convex unconstrained minimization problem

$$\min_\phi \left(G(c, d, \phi) + \int_\Omega \theta\, p(\phi)\, dx\right) \tag{16}$$

where $p(\xi) := \max\{0, 2|\xi - 0.5| - 1\}$, *provided that* $\theta > \frac{1}{2}\|\psi\|_{L^\infty(\Omega)}$ *and* $\|\psi\|_{L^\infty(\Omega)} < +\infty$, *where*

$\psi := \eta + \lambda_{in}|I - c_{in}|^2 - \lambda_{out}|I - c_{out}|^2 + \overline{\lambda}_{in}\left||\nabla I|^s - d_{in}\right|^2 + \overline{\lambda}_{out}\left||\nabla I|^s - d_{out}\right|^2$,
for (2) *and*

$\psi := \eta + \frac{1}{n}\sum_{i=1}^{n}\left(\lambda^i_{in}|I_i - c^i_{in}|^2 - \lambda^i_{out}|I_i - c^i_{out}|^2 + \overline{\lambda}^i_{in}\left||\nabla I_i|^s - d^i_{in}\right|^2 + \overline{\lambda}^i_{out}\left||\nabla I_i|^s - d^i_{out}\right|^2\right)$,
for (5).

Proof: The proof follows the same arguments as in [6], thus we omit it. We just give the key observation for justifying the formulation (13)-(14). Variations of the functional (2), with respect to the level set function ϕ, lead to the steady state equation

$$\begin{aligned}\frac{\partial\phi}{\partial t} &= H'_\epsilon(\phi)\left(\mu\, div\left(\frac{\nabla\phi}{|\nabla\phi|}\right) - \eta - \lambda_{in}|I - c_{in}|^2 + \lambda_{out}|I - c_{out}|^2\right)\\ &+ H'_\epsilon(\phi)\left(-\overline{\lambda}_{in}\left||\nabla I|^s - d_{in}\right|^2 + \overline{\lambda}_{out}\left|\nabla I|^s - d_{out}\right|^2\right),\end{aligned} \tag{17}$$

where in (2) the Heaviside function has been replaced by a noncompact supported, smooth approximation H_ϵ, and H'_ϵ is its derivative (in [9] the choice is $H_\varepsilon(z) := \frac{1}{\pi}\big(\arctan(\frac{z}{\varepsilon}) + \frac{1}{2\varepsilon}\big)$), and $H'_\varepsilon(z) = \frac{\varepsilon}{\pi(\varepsilon^2+z^2)}$). As a result, the steady state solution of (17) coincides with the steady state solution of

$$\begin{aligned}\frac{\partial\phi}{\partial t} &= \mu\, div\left(\frac{\nabla\phi}{|\nabla\phi|}\right) - \eta - \lambda_{in}|I - c_{in}|^2 + \lambda_{out}|I - c_{out}|^2\\ &\quad -\overline{\lambda}_{in}\left||\nabla I|^s - d_{in}\right|^2 + \overline{\lambda}_{out}\left|\nabla I|^s - d_{out}\right|^2.\end{aligned} \tag{18}$$

The conclusion follows by remarking that (18) is the gradient descent scheme for minimizing the functional G in (14). ■

Moreover, we remark that the unconstrained convex minimization problem (16) can be regularized, by adding to the objective functional G the terms indicated in (6), that is, we replace in (16) G by $G_{\alpha\beta}$ where

$$G_{\alpha\beta}(c, d, \phi) := G(c, d, \phi) + \frac{\beta}{4}\int_\Omega \left(|\nabla\phi|^2 - 1\right)^2 dx + \frac{\alpha}{2}\int_\Omega |\nabla\phi|^2\, dx, \tag{19}$$

with $\beta \geq 0$ and $\alpha \geq 0$ two fixed parameters.

4. Numerical solution

For determining the approximate solution to the variational segmentation problem (3), proposed in this paper, we use its reformulation indicated in Proposition 3.2, and, in some cases, with the regularized objective functional

(19), *i.e.* we consider the problem

$$\min_{\phi} \Big(G_{\alpha\beta}(c, d, \phi) + \int_{\Omega} \theta\, p(\phi)\, dx \Big) \tag{20}$$

with $\alpha \geq 0$, $\beta \geq 0$.

The methodology is a two-step scheme. In the first step the values of the unknown averages $c = (c_{in}, c_{out})$ and $d = (d_{in}, d_{out})$ are computed by means of the segmentation function ϕ (see (5) for the scalar segmentation model (2)). In the second step, and using these averages, the minimization of $G_{\alpha\beta}(c, d, .)$ is performed updating the level set function ϕ. The stopping criterium is a pre-defined number of iterations.

The procedure for solving this second step, involves a finite element discretization in space and then a Levenberg-Marquardt Newton-type optimization method (see [11] for more details). More exactly it is a combination of steepest descent (for robustness) and Newton (for quadratic convergence) methods.

A short description of the global scheme is presented below:

Outer loop: 1-: Initialize with given (c^0, d^0) averages and a curve ϕ^0.

Outer loop: 2-: For each $n \geq 0$ and (c^n, d^n) fixed, perform the **Inner loop**, *i.e.*, solve the optimization problem

$$\phi^{n+1} = \min_{\phi} \Big(G_{\alpha\beta}(c, d, \phi) + \int_{\Omega} \theta\, p(\phi)\, dx \Big),$$

using a Levenberg-Marquardt Newton-type optimization method with a variable step length in its gradient descent part (see [11]).

Outer loop: 3-: Update the averages to obtain (c^{n+1}, d^{n+1}) using ϕ^{n+1}. For the case of a scalar image (compare with (4))

$$\begin{aligned} c_{in}^{n+1} &= \frac{\int_{\Omega} I\, H_\epsilon(\phi^{n+1})\, dx}{\int_{\Omega} H_\epsilon(\phi^{n+1})\, dx}, \qquad & c_{out}^{n+1} &= \frac{\int_{\Omega} I \left(1 - H_\epsilon(\phi^{n+1})\right) dx}{\int_{\Omega} \left(1 - H_\epsilon(\phi^{n+1})\right) dx} \\ d_{in}^{n+1} &= \frac{\int_{\Omega} |\nabla I|^s\, H_\epsilon(\phi^{n+1})\, dx}{\int_{\Omega} H_\epsilon(\phi^{n+1})\, dx}, \qquad & d_{out}^{n+1} &= \frac{\int_{\Omega} |\nabla I|^s \left(1 - H_\epsilon(\phi^{n+1})\right) dx}{\int_{\Omega} \left(1 - H_\epsilon(\phi^{n+1})\right) dx}, \end{aligned} \tag{21}$$

where H_ϵ is the regularization of the Heaviside function H (as already mentioned, before, after (17), H is replaced by H_ϵ in (2)). Similar formulas hold for the vector-valued case (with I replaced by I_i).

Outer loop: 4-: Stop when the optimality condition for ϕ is smaller than ϵ_1, in the inner loop, and the difference of two consecutive averages is smaller than ϵ_2, in the outer loop (ϵ_1 and ϵ_2 are two small positive prescribed values).

5. Numerical experiments

We describe now the results obtained both in synthetic and endoscopic images. The spatial domain is $\Omega = [-1, 1]^2$ and is discretized with N^2 finite elements (N is indicated for each image, it depends on the image size). The implementation is done in COMSOL MULTIPHYSICS® [10].

For smoothing the gradient norm $|\nabla I|$, we solve the diffusion equation

$$z - D\Delta z = |\nabla I|, \tag{22}$$

with D the diffusion coefficient (its value is indicated for each image). So the smoothed $|\nabla I|^s$ is the solution z of this equation. When $I = (I_i)_{i=1}^n$ is a vector-valued function we smooth the gradient norm of each component of I, *i.e.* $|\nabla I_i|$.

For all the experiments, $\epsilon = 0.1$ (in the regularized Heaviside function H_ϵ defined after (17)), the regularizing parameter $\eta = 0$, and in the penalty term (16), $\theta = 1$, and p is is replaced by a regularized penalty p_b (we choose $p_b(z) = \frac{z^2}{2b}$, for $z \leq 0$, $p_b(z) = 0$, for $0 < z < 1$, and $p_b(z) = \frac{z^2}{2b} - \frac{z}{b} - \frac{1}{2b}$, for $z \geq 1$, with $b = 0.1$). The parameter μ is always equal to 220/250 for the medical Figures 3, 4, 5, equal to 3 in Figure 1, and to 0.1 in Figure 2. The regularizing parameters α and β are equal to 10^{-9} and 10^{-5} for all the figures (for the gray-scale synthetic image on Figure 1 the values $\alpha = 10^{-9}$ and $\beta = 10^{-7}$ are also used in subfigures (i) and (j)). For the weighting parameters λ and $\overline{\lambda}$, as well for the initial averages $c^0 = (c^0_{in}, c^0_{out})$ and $d^0 = (d^0_{in}, d^0_{out})$, their values are indicated for each image. For RGB images, the order of the components of these parameters and averages, are the red (uperscript 1), green (uperscript 2) and blue channel (uperscript 3). In all the figures the initial contour is a seed of circles.

We observed that, in all the experiments, for the objects displaying many oscillations, the internal contours are obtained with the Chan and Vese model (so, without any gradient norm fitting terms), while the segmentation of the outer boundary of the whole object is achieved with the proposed model, with the extra gradient norm terms (isolated or combined with the other fitting terms). In addition, we also remarked that when α and β are not zero less details are captured, and the model tends to produce a macro segmentation, *i.e.*, a segmentation of the outer boundary of the object, to be detected, without the inner contours.

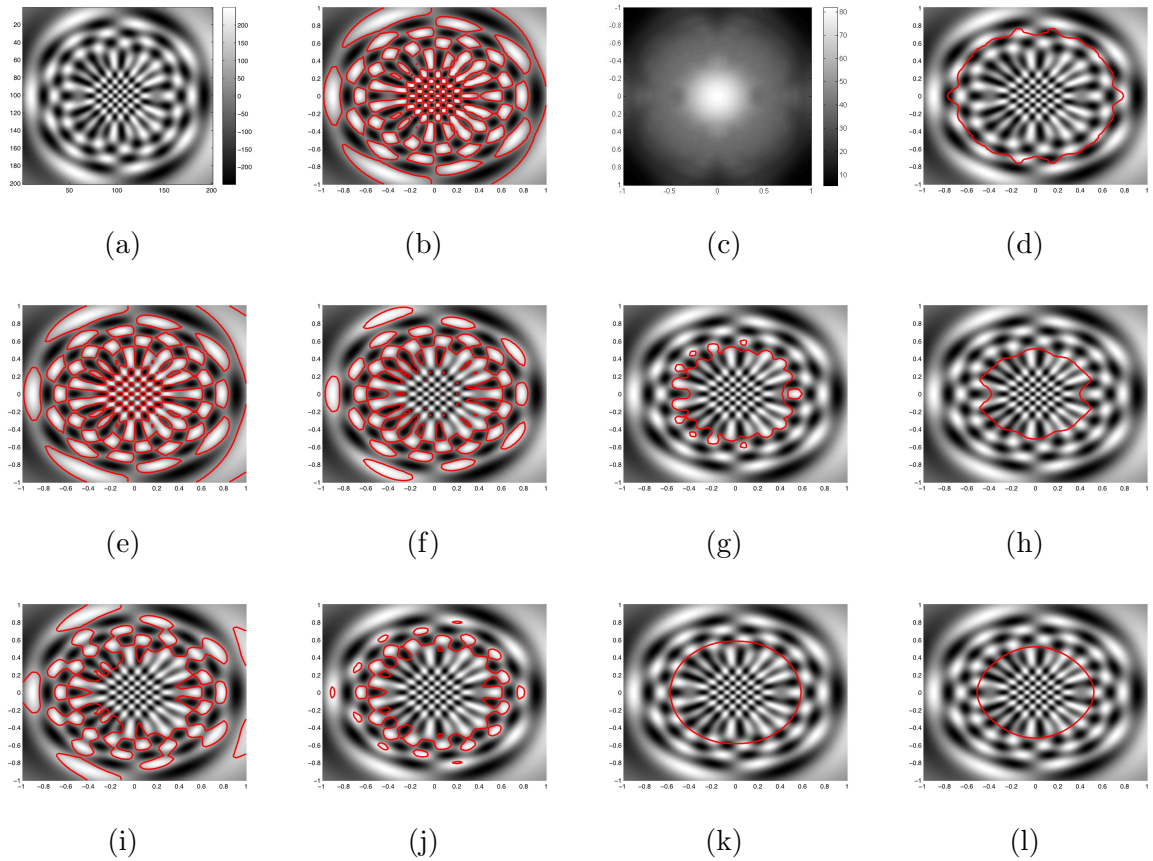

FIGURE 1. Synthetic image (a). Smoothed gradient norm (c). Segmentations (red contours superimposed to the image) without the gradient norm terms in (b) and with the proposed model in (d) to (l). First row: (b) $\lambda = (1,1)$, $\overline{\lambda} = (0,0)$, $\alpha = 0 = \beta$. (c) $D = 10^{-2}$. (d) $\lambda = (0,0)$, $\overline{\lambda} = (50,50)$, $\alpha = 0 = \beta$. Second row, $\alpha = 0 = \beta$: (e) $\lambda = (1,1)$, $\overline{\lambda} = (55,55)$. (f) $\lambda = (1,1)$, $\overline{\lambda} = (70,70)$. (g) $\lambda = (.65,.65)$, $\overline{\lambda} = (75,75)$. (h) $\lambda = (.65,.65)$, $\overline{\lambda} = (150,150)$. Third row $\alpha \neq 0 \neq \beta$ and $\lambda = (1,1)$: (i) $\alpha = 10^{-9}$, $\beta = 10^{-7}$, $\overline{\lambda} = (55,55)$. (j) $\alpha = 10^{-9}$, $\beta = 10^{-7}$, $\overline{\lambda} = (70,70)$. (k) $\alpha = 10^{-9}$, $\beta = 10^{-5}$, $\overline{\lambda} = (75,75)$. (l) $\alpha = 10^{-9}$, $\beta = 10^{-5}$, $\overline{\lambda} = (250,250)$. For all the segmentations, $N = 50^2$, $c^0 = (c^0_{in}, c^0_{out}) = (160,-50)$, $d^0 = (d^0_{in}, d^0_{out}) = (70,30)$; iterations: 4 outer loop and 11 inner loop.

5.1. Synthetic images. The Figure 1 displays the results for a gray-scale synthetic image (with 200×200 pixels), defined by the scalar function

$$I(x,y) := 250 \sin(\exp 3(1-x^2-y^2)\pi x) \cos(\exp 3(1-x^2-y^2)\pi y), \quad (x,y) \in [-1,1]^2.$$

As it can be seen in Figure 1 (b), the single Chan and Vese model does a complete accurate segmentation with the contours detecting all the regions with high values (white in the picture). On the other hand, in (d), which

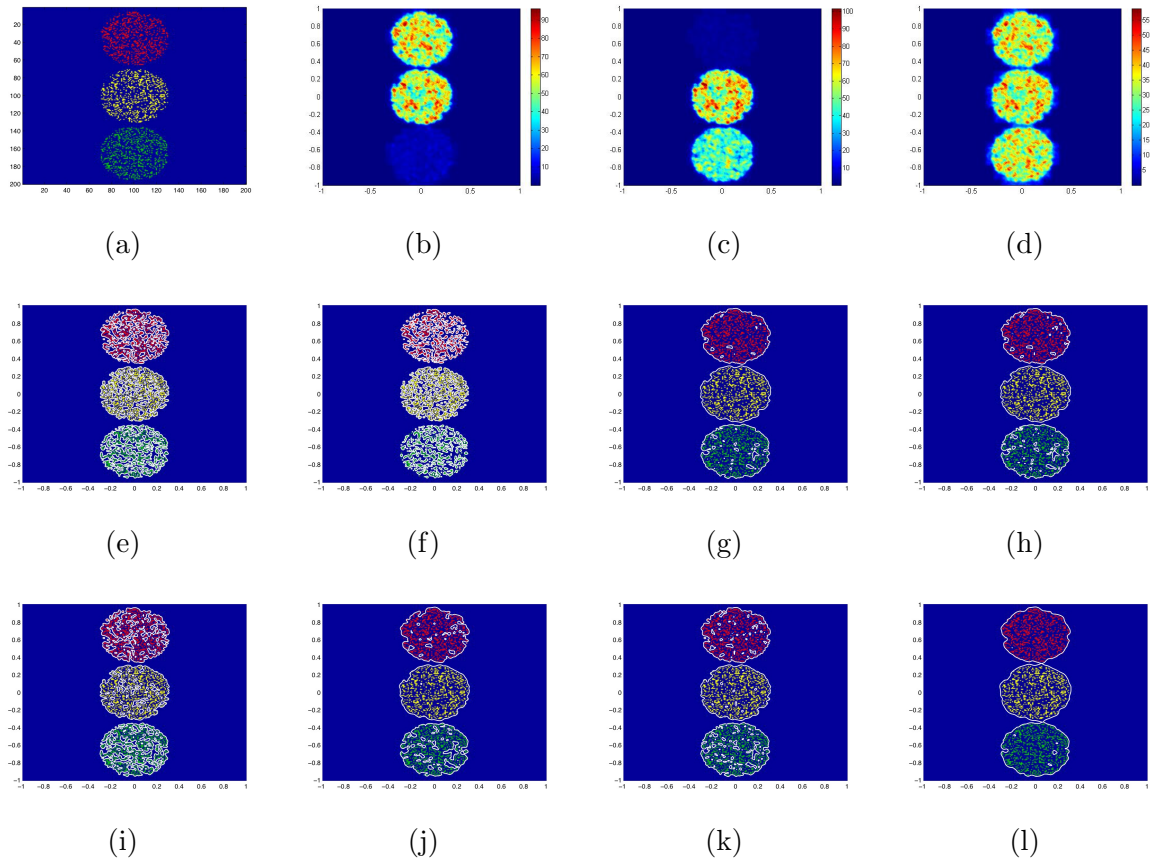

FIGURE 2. Synthetic RGB circles (a). Smoothed gradient norms for the red (b), green (c) and blue (d) channels. Segmentations (white contours over the original image) without the gradient norm terms in (e), (f), (i), (j) and with the proposed model in (g), (h), (k), (l). First row: (b), (c) and (d) $D = 10^{-4}$. Second row, $\alpha = 0 = \beta$, $\lambda^i = (1,1)$: (e) and (f) $\overline{\lambda}^i = (0,0)$. (g) and (h) $\overline{\lambda}^i = (6,6)$. (e), (g) with 4×3 and (f), (h) with 4×7, outer$\times$inner iterations. Third row, $\alpha = 10^{-9}$, $\beta = 10^{-5}$, $\lambda^i = (1,1)$. (i) and (j) $\overline{\lambda}^i = (0,0)$. (k) and (l), $\overline{\lambda}^1 = \overline{\lambda}^2 = (1,1)$, $\overline{\lambda}^3 = (5,3)$. (i), (k) with 4×3 and (j), (l) with 4×7, outer$\times$ inner iterations. For all the segmentations, $N = 190^2$, $c^0_{in} = (50,40,110)$, $c^0_{out} = (2,0,150)$, $d^0_{in} = (35,30,50)$, $d^0_{out} = (0,0,0)$.

displays the segmentation with only the gradient norm terms, it is evident the macro feature of the gradient norm terms. Moreover, if we look from the left to the right on rows 2 and 3, it is evident the macro influence of the gradient terms (the fitting terms $\overline{\lambda}$'s are increasing in that direction from left to right). In addition, if we compare (b) and (e) it is also clear the macro effect of the gradient norm terms: in (e) clearly the contour involves the central part of the image, but it does not segment each tiny (white) dot individually as in (b), it rather segments this central bulk region as a whole,

perfectly, and also it detects some large holes in it, corresponding to lower intensity values (black in the picture). Also, comparing again rows 2 and 3, in the former the regularizing parameters α and β are zero and in the latter not, and it is clear, that these parameters also contribute to reducing the length of the segmentation curve, and thus some details can be missed. This effect of α and β is also verified for the other images described in this section.

The Figure 2 shows a synthetic RGB image in (a), with three circles (200×200 pixels). We observe, that the single Chan and Vese model, without the regularizing terms α, β (see (e) and (f)) does an accurate internal segmentation, inside each circle (we recall we are applying the Levenberg-Marquardt Newton-type optimization method, mentioned in section 4). However it does not generate the macro contour in the external boundary of each circle, even if we increase the iterations. But taking α, β nonzero (see (i) and (j)) it segments the outer boundary of each circle in (j), after 4 outer and 7 inner iterations, and the interior contours tend to disappear (also with more iterations these decrease and then disappear). In subfigures (k) and (l) with took $\overline{\lambda}^3$ bigger than $\overline{\lambda}^1$, $\overline{\lambda}^2$, because the gradient norm of the blue channel contains more information as it can be seen in (d). With the proposed model, we obtain a good and fast macro segmentation (in 4 outer and 3 inner iterations), for all the tests, and in some cases (see (g) and (h)) small tiny interior segmentations are also achieved. More inner contours are possible with the proposed model, together with the macro contour, for suitable choices of $\overline{\lambda}^i_{in}$, $\overline{\lambda}^i_{out}$, α and β.

5.2. Endoscopic images. In this section we present the segmentation results for three medical images (from the Department of Gastroenterology, University Hospital of Coimbra, Portugal), showing aberrant crypt foci (ACF). They are all RGB images, for which we have applied the vector-valued segmentation model described in (5).

The Figure 3 (a) contains two foci: the two dark and roundish regions on the top left and bottom right. Inside each focus the small holes represent the aberrant crypt orifices. The image (a) has 300×300 pixels. By comparing the segmentations of the first row (without the gradient norm terms) with the second row (with the proposed model), in this latter the results are clearly far superior. In effect, in the first row (without the gradient norm terms), we tried to capture accurately the external boundaries of the two foci (by varying the values of λ^i_{in} and λ^i_{out}), but we did not succeed. In contrast, in the second

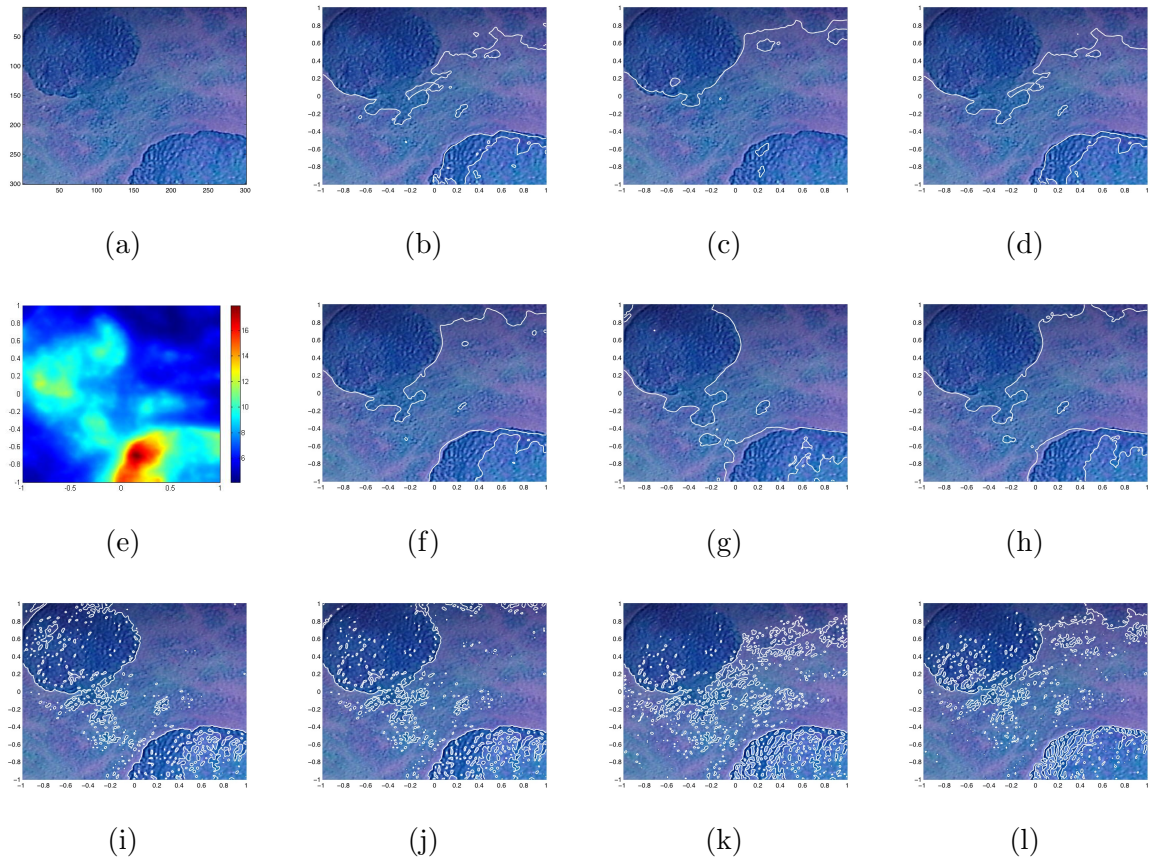

FIGURE 3. Medical image (a) displaying two ACF. Smoothed gradient norm for the green channel (e). Segmentations (white contours overlapping the original image), without the gradient norm terms in (b), (c), (d), (k), (l) and with the proposed model in (f), (g), (h), (i), (j). First row, $\alpha = 10^{-9}$, $\beta = 10^{-5}$, $(\overline{\lambda}^i_{in}, \overline{\lambda}^i_{out}) = (0,0)$ and $(\lambda^i_{in}, \lambda^i_{out})$ equal to $(3,3)$ in (b), $(4,3)$ in (c), and $(5,5)$ in (d). Second row, $\alpha = 10^{-9}$, $\beta = 10^{-5}$, $(\lambda^i_{in}, \lambda^i_{out}) = (3,3)$ and $(\overline{\lambda}^i_{in}, \overline{\lambda}^i_{out})$ equal to $(150,150)$ in (f), to $(175,150)$ in (g), to $(160,160)$ in (h). (e) $D = 10^{-2}$. Third row, $\alpha = \beta = 0$: (i) $(\lambda^i_{in}, \lambda^i_{out}) = (3,3)$ and $(\overline{\lambda}^i_{in}, \overline{\lambda}^i_{out}) = (200,140)$. (j) $(\lambda^i_{in}, \lambda^i_{out}) = (3,3)$ and $(\overline{\lambda}^i_{in}, \overline{\lambda}^i_{out}) = (190,140)$. (k) $(\lambda^i_{in}, \lambda^i_{out}) = (3,3)$ and $(\overline{\lambda}^i_{in}, \overline{\lambda}^i_{out}) = (0,0)$. (l) $(\lambda^i_{in}, \lambda^i_{out}) = (5,3)$ and $(\overline{\lambda}^i_{in}, \overline{\lambda}^i_{out}) = (0,0)$. For all the segmentations, $N = 190^2$, $c^0_{in} = (90,80,160)$, $c^0_{out} = (130,100,200)$, $d^0_{in} = (20,15,10)$, $d^0_{out} = (10,8,5)$; iterations: 4 outer loop and 11 inner loop.

row, the two external boundaries are easily detected by using the proposed model, with the gradient norm terms. In the third row, the regularizing parameters α and β are zero. Obviously there are more details, but again (i), (j) (obtained with the proposed model) are better segmentations than (k), (l) (obtained without the gradient norm terms).

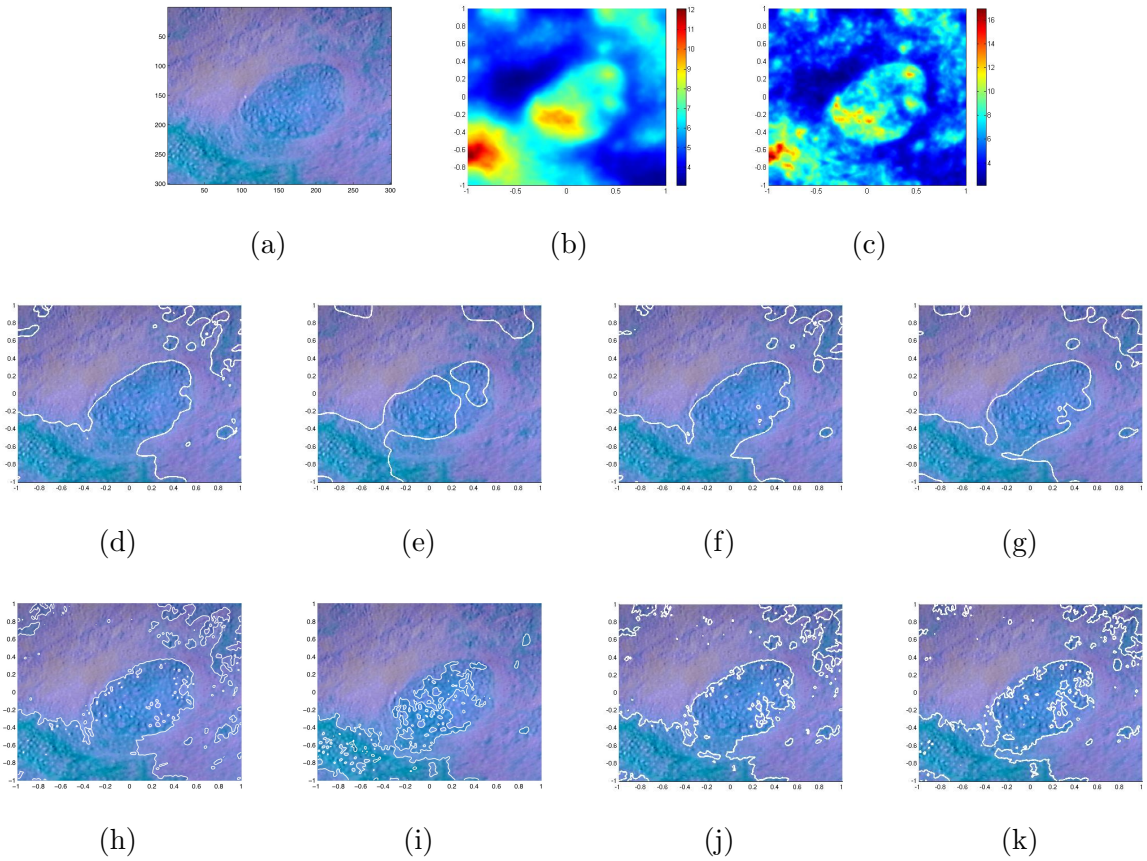

FIGURE 4. Medical endoscopic image(a) displaying one ACF. In (b) and (c) the smoothed gradient norms, for the red channel, with different diffusion coefficients. Segmentations (white contours superimposed to the original image) without the gradient norm terms in (d), (h), (i), with the proposed model in (f), (g), (j), (k), and only with the gradient norm terms in (e). First row: (b) $D = 10^{-2}$ and (c) $D = 10^{-3}$. Second row, $\alpha = 10^{-9}$, $\beta = 10^{-5}$: (e) $(\lambda^i_{in}, \lambda^i_{out}) = (0, 0)$, $(\overline{\lambda}^i_{in}, \overline{\lambda}^i_{out}) = (120, 120)$, $D = 10^{-2}$. (d), (f) and (g), $(\lambda^i_{in}, \lambda^i_{out}) = (3, 3)$ and $(\overline{\lambda}^i_{in}, \overline{\lambda}^i_{out})$ equal to $(0, 0)$ in (d), to $(120, 120)$ in (f) (with $D = 10^{-2}$), and to $(300, 300)$ in (g) (with $D = 10^{-3}$). Third row, $\alpha = \beta = 0$: (h) and (i), $(\overline{\lambda}^i_{in}, \overline{\lambda}^i_{out}) = (0, 0)$ and $(\lambda^i_{in}, \lambda^i_{out})$ equal to $(3, 3)$ in (h), and to $(3, 1)$ in (i). (j) and (k) $D = 10^{-3}$, $(\lambda^i_{in}, \lambda^i_{out}) = (3, 3)$, and $(\overline{\lambda}^i_{in}, \overline{\lambda}^i_{out})$ equal to $(150, 150)$ for (j), and to $(300, 150)$ for (k). For all the segmentations, $N = 200^2$, $c^0_{in} = (90, 150, 200)$, $c^0_{out} = (130, 100, 150)$, $d^0_{in} = (10, 9, 10)$, $d^0_{out} = (15, 3, 5)$; iterations: 4 outer loop and 11 inner loop.

The medical Figure 4 (a) shows another aberrant crypt focus, with oval shape, located in the middle of the image. The image in (a) has 300×300 pixels. In subfigures (f) and (g) we show the difference caused in the segmentations, by using different diffusion coefficients, for smoothing the gradient norms of the given image. It appears that (g), obtained with a bigger

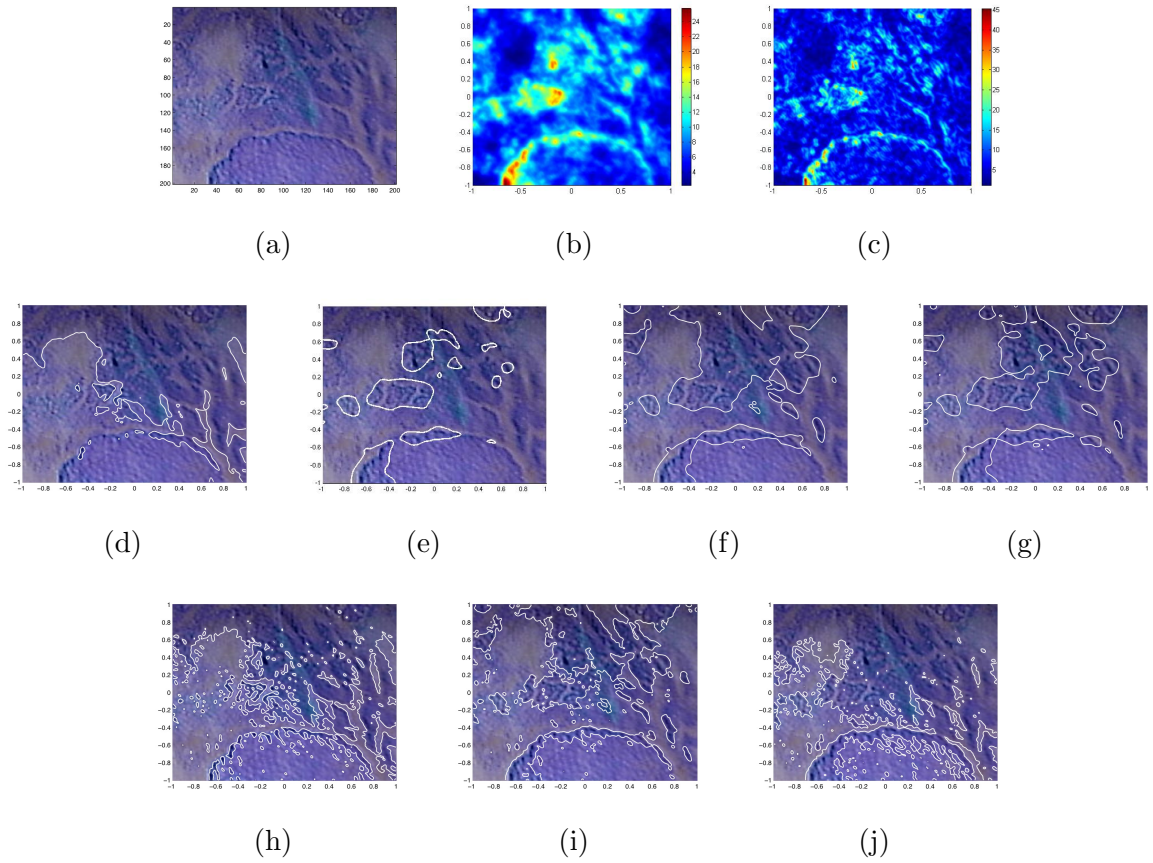

FIGURE 5. Medical endoscopic image (a). Smoothed gradient norms for the red channel with different diffusion coefficients in (b) and (c). Segmentations (white contours over the medical image) without the gradient norm terms in (d), (h), with the proposed model in (f), (g), (i), (j), and with only the gradient norm terms in (e). First row: (b) $D = 10^{-3}$ and (c) $D = 10^{-4}$. Second row, $\alpha = 10^{-9}$, $\beta = 10^{-5}$: (d) $(\lambda^i_{in}, \lambda^i_{out}) = (3,3)$, $(\overline{\lambda}^i_{in}, \overline{\lambda}^i_{out}) = (0,0)$. (f) (with $D = 10^{-3}$) and (g) (with $D = 10^{-4}$), $(\lambda^i_{in}, \lambda^i_{out}) = (3,3)$, $(\overline{\lambda}^i_{in}, \overline{\lambda}^i_{out}) = (150,150)$. (e) $D = 10^{-3}$, $(\lambda^i_{in}, \lambda^i_{out}) = (0,0)$, $(\overline{\lambda}^i_{in}, \overline{\lambda}^i_{out}) = (150,150)$. Third row, $\alpha = \beta = 0$: (h) $(\lambda^i_{in}, \lambda^i_{out}) = (3,3)$, $(\overline{\lambda}^i_{in}, \overline{\lambda}^i_{out}) = (0,0)$. (i) and (j) $D = 10^{-3}$, $(\lambda^i_{in}, \lambda^i_{out}) = (3,3)$, and $(\overline{\lambda}^i_{in}, \overline{\lambda}^i_{out})$ equal to $(150,150)$ for (i), and to $(10,200)$ for (j). For all the segmentations, $N = 190^2$, $c^0_{in} = (90,80,160)$, $c^0_{out} = (130,100,200)$, $d^0_{in} = (20,15,10)$, $d^0_{out} = (10,8,5)$; iterations: 4 outer loop and 11 inner loop.

diffusion coefficient, is better than (f). By comparing the segmentations of the second row (all with $\alpha = 10^{-9}$ and $\beta = 10^{-5}$), again (f) and (g) obtained with the proposed model is better than the segmentation in (d), without the gradient norm terms. In (e), where only the gradient norm terms are used, the segmentation does not produce a very good result; though it is in good agreement with the input data (the gradient norm of the red channel of the

input data is shown in (b)). In the third row, the regularizing parameters α and β are zero, (h) and (i) are obtained without the gradient norm terms, and (j), (k) with the proposed model. In (i) the fitting parameters verify $\lambda^i_{in} > \lambda^i_{out}$ and in (k) also $\overline{\lambda}^i_{in} > \overline{\lambda}^i_{out}$, causing the segmentation to be reinforced inside the focus. But by comparing (i) and (k), it is clear (k), which includes the gradient norm terms, is superior.

The medical Figure 5 (a) contains another aberrant crypt focus (the large semi-circular region at the bottom) and possible other aberrant crypts (the dark regions going down from the top to the beginning of the focus). The image in (a) has 200×200 pixels. This last medical Figure 5 demonstrates once again that the segmentation with the proposed model in (f), (g), (i), (j) is better by comparison with the segmentations in (d), (h), where the gradient norm terms are not used. We remark that (e) (obtained with only the gradient norm terms) give a good segmentation of the gradient norm image, which is the input data (its red channel is displayed in (b)); the same type of result is obtained in Figure 4 (e).

6. Conclusions and future work

A variational segmentation model is proposed. It is a generalization of the Chan and Vese model (for both the scalar and vector-valued cases), that incorporates additional fitting terms involving the image gradient norm. As a consequence, an overall macro-micro segmentation model is obtained as demonstrated in the results for synthetic and endoscopic medical images. Moreover, on the whole, these results also show the superiority of the segmentation with the proposed model compared to the segmentation performed with the single Chan and Vese model. This was expected since the proposed model embodies much more information from the input image than the single Chan and Vese model.

In addition, theoretical existence results, as well as, the existence of global minimizers (for both the scalar and vector-valued cases) are proven, for the model.

As far as the numerical approximation is concerned, we use a Levenberg-Marquardt Newton-type optimization method, applied to the finite element discretization of the model, as we already did in [11], which has proven to give good results. Other choices are possible, as for instance a split Bregman algorithm as suggested in the recent paper [13].

In the literature there are many extensions of the original Chan and Vese model [9] (as for instance, and just to mention a few, the multiphase model [24], which aims at segmenting images with more than two regions, and [16] which uses local, instead of global, binary fitting terms, thus allowing the possibility of segmenting images with intensity inhomogeneity and multiple means of pixel intensity). Thus, and in light of the model proposed in this paper, straightforward enhancements of these extensions could be achieved by considering extra image gradient norm terms, as we did here in this paper. In the future we intend to address these issues.

References

[1] D. G. Adler, C. J. Gostout, D. Sorbi, et al. Endoscopic identification and quantification of the aberrant crypt in the human colon. *Gastrointestinal Endoscopy*, 56:657–662, 2002.

[2] H. Attouch, G. Buttazzo, and G. Michaille. *Variational analysis in Sobolev and BV spaces*, volume 6 of *MPS/SIAM Series on Optimization*. Society for Industrial and Applied Mathematics (SIAM), Philadelphia, PA, 2006. Applications to PDEs and optimization.

[3] G. Aubert and P. Kornprobst. *Mathematical problems in image processing*, volume 147 of *Applied Mathematical Sciences*. Springer, New York, second edition, 2006. Partial differential equations and the calculus of variations, With a foreword by Olivier Faugeras.

[4] X. Bresson, S. Esedöglu, P. Vandergheynst, J.-P. Thiran, and S. Osher. Fast global minimization of the active contour/snake model. *J. Math. Imaging Vision*, 28(2):151–167, 2007.

[5] V. Caselles, R. Kimmel, and G. Sapiro. Geodesic active contours. *International Journal of Computer Vision*, 22(1):61–79, 1997.

[6] T. F. Chan, S. Esedöglu, and M. Nikolova. Algorithms for finding global minimizers of image segmentation and denoising models. *SIAM J. Appl. Math.*, 66(5):1632–1648 (electronic), 2006.

[7] T. F. Chan, B. Y. Sandberg, and L. A. Vese. Active contours without edges for vector-valued images. *Journal of Visual Communication and Image Representation*, 11(2):130–141, 2000.

[8] T. F. Chan and J. Shen. *Image processing and analysis*. Society for Industrial and Applied Mathematics (SIAM), Philadelphia, PA, 2005. Variational, PDE, wavelet, and stochastic methods.

[9] T. F. Chan and L. A. Vese. Active contours without edges. *IEEE Trans. Image Processing*, 10(2):266–277, 2001.

[10] Comsol Multiphysics®. *http://www.comsol.com/*.

[11] I. N. Figueiredo, P. N. Figueiredo, G. Stadler, O. Ghattas, and A. Araújo. Variational image segmentation for endoscopic human colonic aberrant crypt foci. *IEEE Transactions on Medical Imaging*, 29(4):998–1011, 2010.

[12] E. Giusti. *Minimal surfaces and functions of bounded variation*, volume 80 of *Monographs in Mathematics*. Birkhäuser Verlag, Basel, 1984.

[13] T. Goldstein, X. Bresson, and S. Osher. Geometric applications of the split Bregman method: Segmentation and surface reconstruction. *Journal of Scientific Computing*, pages 1–22, 2009. 10.1007/s10915-009-9331-z.

[14] M. Kass, A. Witkin, and D. Terzopoulos. Snakes: Active contour models. *Int. J. Comput. Vis.*, 1:321–331, 1988.

[15] S. Kichenassamy, A. Kumar, P. Olver, A. Tannenbaum, and A. Yezzi, Jr. Conformal curvature flows: from phase transitions to active vision. *Arch. Rational Mech. Anal.*, 134(3):275–301, 1996.

[16] C. Li, C. Kao, J. Gore, and Z. Ding. Implicit active contours driven by local binary fitting energy. In *Proceedings of IEEE Conference on Computer Vision and Pattern Recognition (CVPR)*, pages 1–7, Washington, DC, USA, 2007. IEEE Computer Society.

[17] R. Malladi, J. A. Sethian, and B. C. Vemuri. Shape modeling with front propagation: a level set approach. *IEE Transactions on Pattern Analysis and Machine Intelligence*, 17(2):158–175, 1995.

[18] J.-M. Morel and S. Solimini. *Variational Methods in Image Processing*. Birkhauser, Boston, USA, 1994.

[19] D. Mumford and J. Shah. Optimal approximations by piecewise smooth functions and associated variational problems. *Comm. Pure Appl. Math.*, 42(5):577–685, 1989.

[20] S. Osher and R. Fedkiw. *Level set methods and dynamic implicit surfaces*, volume 153 of *Applied Mathematical Sciences*. Springer-Verlag, New York, 2003.

[21] S. Osher and J. A. Sethian. Fronts propagating with curvature-dependent speed: algorithms based on Hamilton-Jacobi formulations. *J. Comput. Phys.*, 79(1):12–49, 1988.

[22] L. Roncucci, A. Medline, and W. R. Bruce. Classification of aberrant crypt foci and microadenomas in human colon. *Cancer Epidemiology, Biomarkers & Prevention*, 1:57–60, 1991.

[23] T. Takayama, S. Katsuki, Y. Takahashi, et al. Aberrant crypt foci of the colon as precursors of adenoma and cancer. *The New England Journal of Medicine*, 339:1277–1284, 1998.

[24] L. Vese and T. F. Chan. A multiphase level set framework for image segmentation using the Mumford and Shah model. *International Journal of Computer Vision*, 50(3):271–293, 2002.

[25] N. Zhang, J. Zhang, and R. Shi. An improved Chan-Vese model for medical image segmentation. In *2008 International Conference on Computer Science and Software Engineering*, volume 1, pages 864–867, 2008.

Isabel N. Figueiredo
CMUC, Department of Mathematics, University of Coimbra, 3001-454 Coimbra, Portugal.
E-mail address: isabelf@mat.uc.pt

Juan Moreno
CMUC, Department of Mathematics, University of Coimbra, 3001-454 Coimbra, Portugal.
E-mail address: jmoreno@mat.uc.pt

Surya Prasath
CMUC, Department of Mathematics, University of Coimbra, 3001-454 Coimbra, Portugal.
E-mail address: surya@mat.uc.pt

Pedro Figueiredo
Faculty of Medicine, University of Coimbra, 3004-504 Coimbra, and Department of Gastroenterology, University Hospital of Coimbra, 3000-075 Coimbra, Portugal.
E-mail address: pedro.n.figueiredo@clix.pt